minerals

MDPI

Article

Muscovite Dehydration Melting in Silica-Undersaturated Systems: A Case Study from Corundum-Bearing Anatectic Rocks in the Dabie Orogen

Yang Li [1], Yang Yang [1], Yi-Can Liu [1,*], Chiara Groppo [2,3] and Franco Rolfo [2,3]

[1] CAS Key Laboratory of Crust-Mantle Materials and Environments, School of Earth and Space Sciences, University of Science and Technology of China, Hefei 230026, China; ly20115@mail.ustc.edu.cn (Y.L.); chanming@mail.ustc.edu.cn (Y.Y.)

[2] Department of Earth Sciences, University of Torino, Via Valperga Caluso 35, 1-10125 Torino, Italy; chiara.groppo@unito.it (C.G.); franco.rolfo@unito.it (F.R.)

[3] Consiglio Nazionale delle Ricerche-Istituto di Geoscienze e Georisorse, Section of Torino, Via Valperga Caluso 35, 1-10125 Torino, Italy

* Correspondence: liuyc@ustc.edu.cn; Tel.: +86-551-6360-0367

Received: 17 January 2020; Accepted: 24 February 2020; Published: 27 February 2020

Abstract: Corundum-bearing anatectic aluminous rocks are exposed in the deeply subducted North Dabie complex zone (NDZ), of Central China. The rocks consist of corundum, biotite, K-feldspar and plagioclase, and show clear macro- and micro-structural evidence of anatexis by dehydration melting of muscovite in the absence of quartz. Mineral textures and chemical data integrated with phase equilibria modeling, indicate that coarse-grained corundum in leucosome domains is a peritectic phase, reflecting dehydration melting of muscovite through the reaction: Muscovite = Corundum + K-feldspar + Melt. Aggregates of fine-grained, oriented, corundum grains intergrown with alkali feldspar in the mesosome domains are, instead, formed by the dehydration melting of muscovite with aluminosilicate, through the reaction: Muscovite + Al-silicate = Corundum + K-feldspar + Melt. P-T pseudosections modeling in the Na_2O-CaO-K_2O-FeO-MgO-Al_2O_3-SiO_2-H_2O-TiO_2 system constrains peak pressure-temperature (P-T) conditions at 900–950 °C, 9–14 kbar. The formation of peritectic corundum in the studied rocks is a robust petrographic evidence of white mica decompression melting that has occurred during the near-isothermal exhumation of the NDZ. Combined with P-T estimates for the other metamorphic rocks in the area, these new results further confirm that the NDZ experienced a long-lived high-T evolution with a near-isothermal decompression path from mantle depths to lower-crustal levels. Furthermore, our new data suggest that white mica decompression melting during exhumation of the NDZ was a long-lasting process occurring on a depth interval of more than 30 km.

Keywords: corundum; anatexis; silica-undersaturated muscovite dehydration melting; phase equilibria modelling; deeply subducted continental crust; aluminous gneiss

1. Introduction

Partial melting of high-pressure (HP) and ultrahigh-pressure (UHP) metamorphic rocks can significantly influence the tectonothermal evolution of collisional orogens, the geochemical differentiation of the continental crust and crust-mantle interaction dynamics within subduction zones [1–3]. Partial melting of deeply buried continental crust at mid- to lower-crustal depths also has critical effects on weakening rocks and promoting deformation, thus playing an important role in evolutional processes of continental collision orogens [4].

In collisional orogens, anatexis can occur at different metamorphic stages, both during continental subduction (i.e., during heating) and during exhumation (i.e., during decompression) [5,6]. Decompression- and heating-melting events [7–14] can be either related to water-fluxed melting (i.e., fluid-present melting) or to dehydration melting (i.e., fluid-absent melting) [15–19]. Dehydration melting generally involves the breakdown of muscovite and biotite in metasedimentary and granitic protoliths [12,20,21]. Fluid-absent melting of muscovite at the amphibolite- to granulite-facies transition marks the onset of deep crustal anatexis, thus is the first dominant mechanism of granitic melt generation in orogenic hinterlands [21–23]. In dry (vapour-absent) crust, muscovite reacts with quartz to produce K-feldspar, aluminosilicate and a monzogranitic melt (Ms + Qz = Kfs + Als + Melt) [15,21,24]. The melting behavior of muscovite in silica-saturated (quartz-present) rocks has been extensively studied based on natural examples, experiments, and thermodynamic modelling [15,20,24,25]. Silica-saturated systems are representative of most crustal rocks, either of metasedimentary or magmatic origin; however, silica-undersaturated anatectic rocks can also occur. For example, silica-undersaturated assemblages have been reported for anatectic rocks derived from quartz-poor pelitic precursors, in which melting and melt loss processes led to the complete exhaustion of quartz and ultimately to the formation of corundum-bearing assemblages [26–29]. Although interest in the study of silica-undersaturated rocks from the base of orogenically thickened crust has progressively increased in recent years, due to their potentiality of providing independent P-T constraints on ultrahigh-temperature (UHT) and high-pressure granulitic (HPG) metamorphism [30–34], studies on muscovite dehydration melting in silica-undersaturated rocks are still scarce.

Corundum (Al_2O_3) is a relatively rare metamorphic mineral that requires unusual silica-undersaturated and high aluminous compositions [35]. Depending on the bulk rock composition, corundum is stable at various P-T conditions, ranging from amphibolite to granulite-facies conditions [36]. In high-grade metamorphic terranes, proposed mechanisms for corundum formation include hydrothermal alteration [37–39], metasomatic exchange of silica with ultramafic rocks [40–42], and anatexis of quartz-poor aluminous protoliths [22,27,36,43]. In this regard, corundum-bearing anatectic rocks are the perfect textbook example to explore partial melting processes in silica-undersaturated systems [22,44].

In this paper, we report the occurrence of corundum-bearing aluminous rocks from the deeply subducted slice of the Dabie orogen, in Central China. Petrographic observation and phase equilibria modeling suggest that dehydration melting of muscovite in the studied rocks occurred in a silica-undersaturated system during isothermal decompression. The main purpose of this study was to clarify the mechanisms responsible for the formation of corundum in such a system, and to discuss their implications for partial melting during exhumation of UHP terranes.

2. Geological Setting and Samples

2.1. Dabie Orogen

The Dabie orogen is one of the most extensively exposed and well-preserved UHP metamorphic terranes in the world. It is located in the central portion of the Qinling-Dabie-Sulu orogenic belt, which resulted from the Triassic continental collision between the North China Block and South China Block [45,46] (Figure 1). UHP metamorphism has been recognized by the occurrence of index minerals such as coesite and microdiamond from various metamorphic rocks [46–49]. The Dabie orogen comprises several fault-bounded terranes with varying metamorphic grades and evolutional histories. It is generally subdivided into five major lithotectonic units from north to south [49–51]: (1) the Beihuaiyang zone (BZ); (2) the North Dabie complex zone (NDZ); (3) the Central Dabie UHP metamorphic zone (CDZ); (4) the South Dabie low-temperature eclogite zone (SDZ); and (5) the Susong complex zone (SZ). These zones are separated by the Xiaotian-Mozitan fault, Wuhe-Shuihou fault, Hualiangting-Mituo fault and Taihu-Shanlong fault, respectively. Among them, the BZ and SZ are two

relatively low-grade composite units, whereas the other zones belong to the deeply subducted South China Block [52–54].

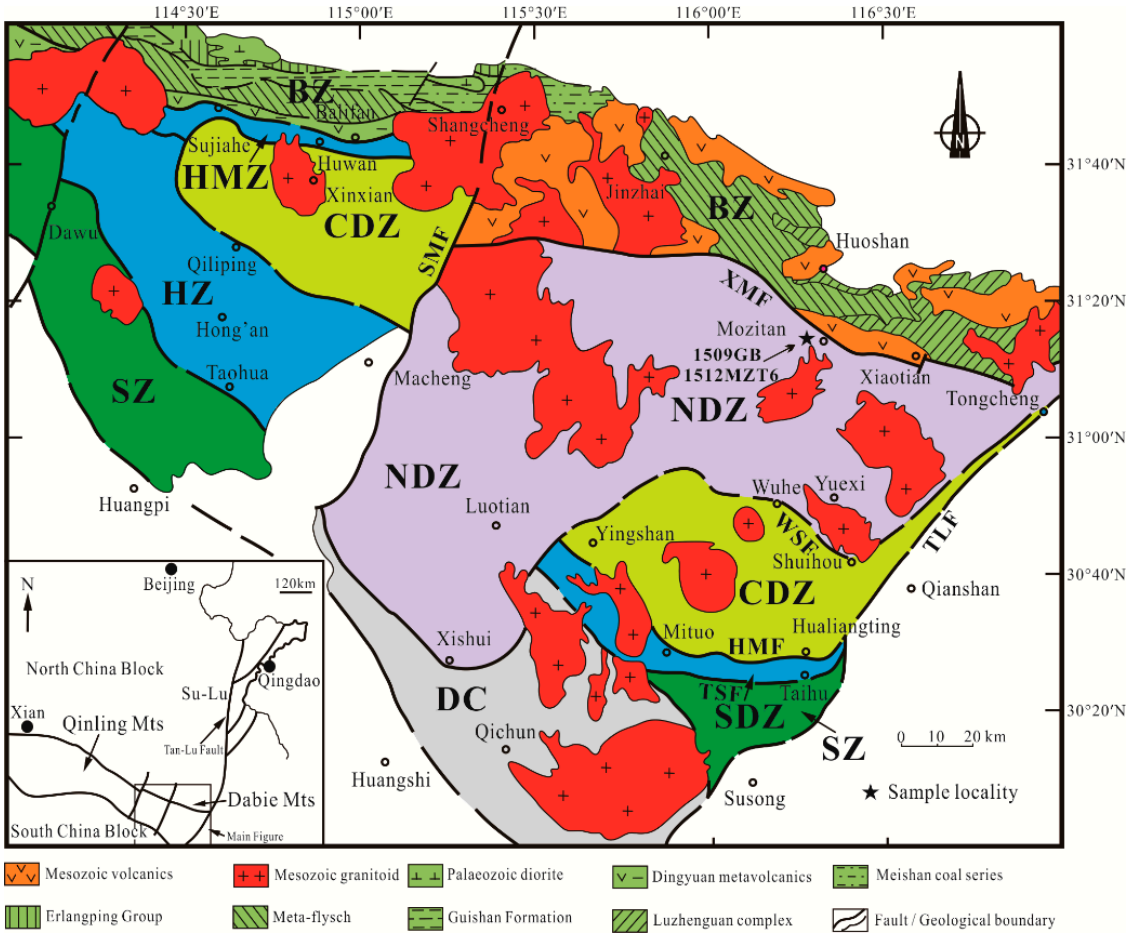

Figure 1. Schematic geological map of the Dabie orogen, with the inset showing the location of this area within the Triassic Qinling-Dabie-Sulu collision orogen in Central China (modified from reference [51]). Sampling locality is marked by a little black star. BZ, Beihuaiyang zone; NDZ, North Dabie high-T/UHP complex zone; CDZ, Central Dabie mid-T/UHP metamorphic zone; SDZ, South Dabie low-T eclogite zone; SZ, Susong complex zone; HMZ, Huwan mélange zone; HZ, Hong'an low-T eclogite zone; DC, amphibolite-facies Dabie complex; XMF, Xiaotian-Mozitan fault; WSF, Wuhe-Shuihou fault; HMF, Hualiangting-Mituo fault; TSF, Taihu-Shanlong fault; TLF, Tan-Lu fault.

The SDZ, CDZ and NDZ are three eclogite-bearing units of the Dabie orogen [46,49,51,55–58]. The occurrence of diamond and coesite in the metamorphic rocks from the CDZ indicates that the UHP metamorphism occurred at 700–850 °C and >2.8 GPa [46–48,59,60], whereas the peak P-T conditions of the eclogites in the SDZ were estimated at 670 °C and 3.3 GPa [56]. In both the CDZ and SDZ units the UHP eclogite-facies stage was followed by HP eclogite- and amphibolite-facies retrograde metamorphism. The NDZ is different from the other two UHP units in two main aspects [61]. Firstly, the NDZ underwent a long-lasting HT granulite-facies metamorphic overprint, while the SDZ and CDZ only underwent amphibole-facies retrogression after eclogite-facies metamorphism [51,62,63]. Secondly, migmatites, especially stromatic migmatites with various leucosomes [64–67] are widespread in the NDZ.

2.2. North Dabie Zone

The NDZ is located between the BZ and CDZ, separated by the Xiaotian-Mozitan fault (XMF) in the north and Wuhe-Shuihou fault (WSF) in the south, respectively (Figure 1). The NDZ is characterized by the exposure of abundant high-T metamorphic rocks of lower crustal origin, mainly consisting of tonalitic to granitic orthogneisses with varying extents of migmatitization and post-collisional Cretaceous intrusions, with subordinate meta-peridotites, garnet-bearing amphibolites and eclogites [51,63,64]. The oriented mineral exsolutions in garnet and clinopyroxene, and the occurrence of micro-diamonds inclusions in zircon and garnet imply that the NDZ eclogites underwent UHP metamorphism at P > 3.5 GPa [49,50,57,58,64,68]. The Triassic zircon U-Pb ages and Sm-Nd ages of the eclogites from the NDZ suggest that these rocks were formed by the Triassic subduction of the South China Block, similar to those from the CDZ and SDZ [45,56,64]. The Triassic metamorphic age and microdiamond inclusions in zircon and garnet from the NDZ banded gneisses suggest that the gneisses hosting the eclogites were also involved in the Triassic deep subduction of the South China Block, thus implying that the NDZ experienced UHP metamorphism as a coherent unit [57,58,63,64,68,69]. Differently from the CDZ and the SDZ, in which the UHP/HP eclogite-facies stage was followed by cooling and decompression under amphibolite-facies conditions, the NDZ experienced a pervasive granulite-facies overprinting accompanied by extensive partial melting and migmatization that partially or completely obliterated the evidence of the earlier metamorphic events at HP/UHP conditions [63,70]. In spite of this pervasive HT overprinting, in the last twenty years an increasing number of UHP/HP eclogite relics have been reported from the NDZ [49–51,57,69,71]. In addition, geochronological studies also indicate that the protoliths of the metamorphic rocks are mostly Neoproterozoic igneous rocks [51,64].

Partial melting of UHP metamorphic rocks from the NDZ has been identified and characterized thanks to the study of multiple generations of leucosomes [4,65–67,70]. Recently, the leucosomes within the migmatites in the NDZ were documented to be formed at ~209 Ma and 143–110 Ma, in response to (i) decompression melting under granulite-facies conditions during exhumation, and (ii) heating melting during post-orogenic collapse, respectively [72]. Moreover, the Sr-Nd-Pb isotope compositions suggest that all the leucosomes have a similar source from the Triassic subducted lower-crustal rocks [72]. Most of the present data point to a complex multistage evolution of the NDZ, characterized by a nearly isothermal decompression at HT/UHT conditions following the UHP metamorphic peak [63,70].

2.3. Studies Samples

The corundum-bearing aluminous rocks (samples 1512MZT6 and 1509GB) investigated in this study occur as lenses within strongly mylonitized granitic gneisses from the Mozitan area in the north portion of the NDZ. At the outcrop scale, the corundum-bearing aluminous rocks have the appearance of stromatic migmatites. Corundum porphyroblasts are ubiquitous and their grain-size distribution is heterogeneous. Smaller, <1 cm size, corundum are preferably found in the weakly foliated mesosome consisting of feldspar and biotite, whereas larger, centimetric, corundum are commonly found in the leucosome, associated with coarse grained K-feldspar (Figure 2). The sampling locations are marked by a little black star in Figure 1.

Figure 2. Field photographs of the corundum-bearing anatectic aluminous rocks exposed in the NDZ. (**a**) The boudin of corundum-bearing rocks included in the granitic gneiss (sample 1512MZT6). (**b**) Detail of the corundum-bearing rock (sample 1512MZT6). (**c**) Sample 1509GB: corundum occurs as single euhedral crystals centered in the coarse-grained leucosomes consisting of K-feldspar.

3. Analytical Method

3.1. Whole-Rock Analysis

Bulk-rock major-element compositions of the studied samples were analyzed by the conventional wet chemical method at the Hebei Institute of Regional Geology and Mineral Resources, China. SiO_2 and loss on ignition (LOI) were determined by gravimetric methods using a P1245 electronic analytical balance. Al_2O_3, CaO, MgO and FeO were determined by titration method. TiO_2, Fe_2O_3 and P_2O_5 were measured by a 722N spectrophotometer. K_2O and Na_2O were measured by a 6400-flame photometer, while MnO was detected by a WFX-110B atomic absorption spectrophotometer. Analytical uncertainties are better than 1%.

3.2. Micro-X-ray Fluorescence (μ-XRF) Maps of the Thin Sections

Qualitative major element X-ray maps of whole thin sections were conducted with Bruker M4 TORNADO equipment (BRUKER Ltd., Hamburg, Germany), located at the CAS Key Laboratory of Crust-Mantle Materials and Environments in the University of Science and Technology of China (USTC), Hefei, China. The operating conditions were 100 ms counting time, 50 kV accelerating voltage and a probe current of 200 μA. The spatial resolution was about 20 μm in both x and y directions. The mineral distribution maps and modal proportion were obtained by processing the raw data with software ARMICS (BRUKER Ltd., Hamburg, Germany).

3.3. Mineral Chemistry

Mineral composition was determined by using a JEOL JXA-8230 electron microprobe (EPMA, JEOL Ltd., Tokyo, Japan) at the School of Resources and Environmental Engineering, Hefei University

of Technology, China. The quantitative analysis was performed using operating conditions of 15 kV accelerating voltage, ~20 nA beam current, peak counting time 10 s, background counting time 5 s and a beam diameter of 3 μm. Standards for this laboratory were natural and synthetic minerals (GB/T 17359-1998; SPI 02753-AB 53 Minerals Standard). The ZAF corrections were applied. The analytical precision was generally better than 2%. Mineral abbreviations used throughout the text, figures and tables are after [73].

4. Petrography and Mineral Chemistry

The two studied samples had similar bulk compositions (Table 1), and consisted of corundum, alkali-feldspar and biotite, with minor amounts of plagioclase. The modal percentages of each mineral were obtained from qualitative major elements X-ray maps extended over all the thin sections. The two samples differed on the ratio between the leucocratic and the mesocratic domains: sample 1512MZT6 was dominated by leucocratic domains, whereas in sample 1509GB the mesocratic domains prevailed (Figure 3). Furthermore, sample 1509GB contained more plagioclase than sample 1512MZT6, in agreement with the measured bulk compositions of the two samples.

Table 1. Whole-rock chemical compositions of corundum-bearing rocks in wt% (**a**) and Effective bulk compositions of 1509GB used for phase diagram modelling in mol% (**b**).

a	**Bulk Composition**		**b**	**Modeling Composition**
	(wt%)			**(mol%)**
	1512MZT6	1509GB		1509GB
SiO_2	49.89	51.72	SiO_2	51.17
Al_2O_3	28.62	25.98	Al_2O_3	14.45
TiO_2	0.81	1.04	TiO_2	1.81
Fe_2O_3	0.77	0.49	FeO	6.24
FeO	3.83	2.83	CaO	0.08
CaO	0.21	0.40	MgO	10.93
MgO	2.45	3.28	K_2O	7.64
K_2O	9.86	9.41	Na_2O	1.36
Na_2O	1.71	2.36	H_2O	6.32
MnO	0.03	0.03	Total	100
P_2O_5	0.01	0.01		
LOI	1.14	1.05		
Total	99.33	98.59 [1]		
Ba (ppm)	5748	12,900		

[1] The difference from 100% may have resulted from a lot of feldspars with high Ba contents in the samples.

4.1. Petrography of Leucosomes and Mesosomes

The studied corundum-bearing gneisses showed a migmatitic structure consisting of variably deformed leucocratic and mesocratic domains. The coarse-grained leucocratic domains consisted of K-feldspar and corundum and they were interpreted as leucosomes; the fine-grained mesocratic domains mostly consisted of biotite, feldspar and corundum and they were interpreted as mesosomes.

Cm-sized, euhedral crystals of corundum systematically occurred in the central parts of the leucosomes (Figures 3 and 4a,b); they were surrounded by coarse-grained perthitic alkali feldspars (which include relics of biotite and plagioclase; Figure 5f), with which they showed equilibrium relationships (Figures 4b and 5f). Rutile and zircon occurred as accessory phases in the corundum porphyroblasts (Figure 4a). The euhedral shapes of rutile and zircon crystals indicated that these minerals crystallized from the melt. In some domains, rounded relict muscovite inclusions were found in the core of the corundum porphyroblasts (Figure 5e).

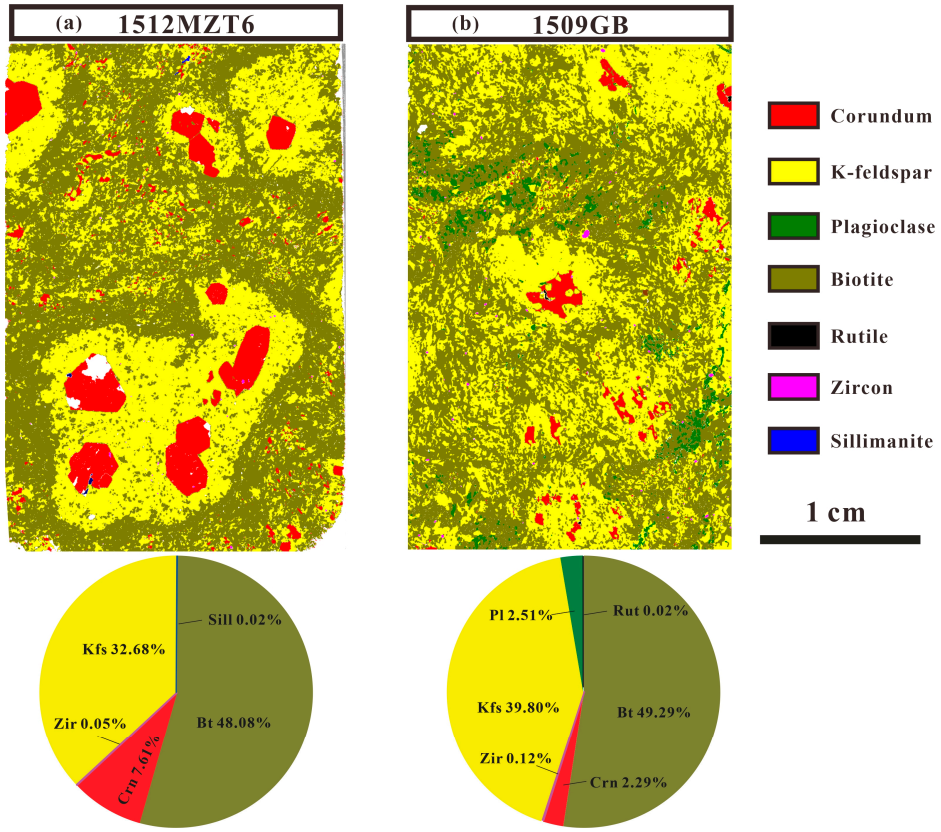

Figure 3. Major element μ-XRF maps of whole thin sections of the studied samples 1512MZT6 (**a**) and 1509GB (**b**). The legend shows the mineral proportions in each sample. White zones are holes through which the thin section glass was analyzed.

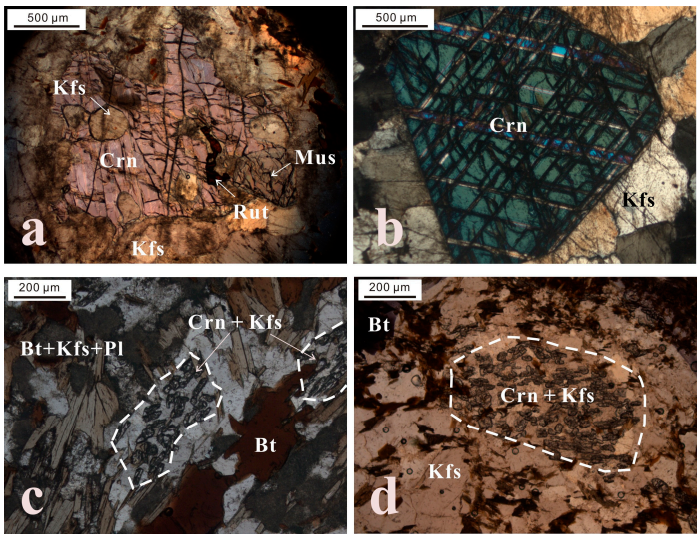

Figure 4. Representative photomicrographs of samples 1509GB and 1512MZT6 viewed in: PPL, plane-polarized light; XPL, crossed-polarized light. (**a**) Large corundum porphyroblast surrounded by K-feldspar and including relic muscovite (sample 1509GB; PPL). (**b**) Euhedral corundum porphyroblast in a coarse-grained aggregate of alkali feldspar in the leucosome (sample 1512MZT6; XPL). (**c**,**d**) Clusters of oriented grains of corundum intergrown with K-feldspar occurring in the mesosome domain (**c**: sample 1509GB; **d**: sample 1512MZT6; PPL).

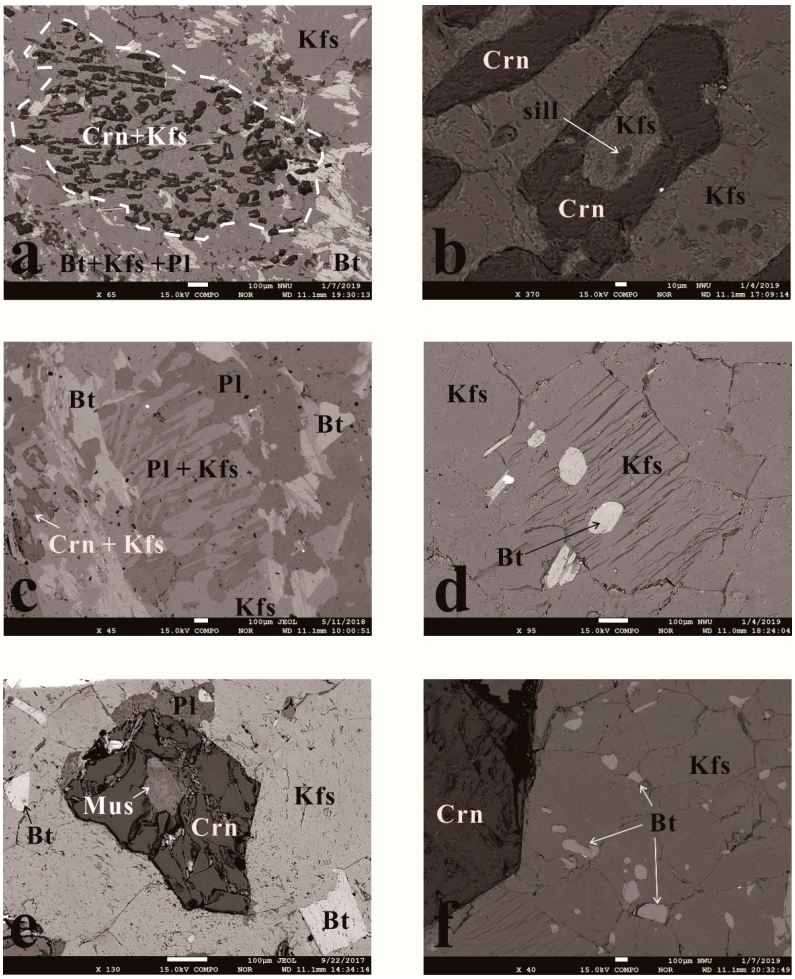

Figure 5. Back-scattered electron (BSE) images of mineral textures in the leucosome and mesosome. (**a**) Detail of the clusters of small Crn+Kfs-intergrowths in the mesosome domain (sample 1512MZT6). (**b**) Enlarged view of (**a**), showing a composite inclusion of resorbed sillimanite rimmed by K-feldspar in corundum. (**c**,**d**) Feldspar perthite texture showing the exsolution lamellae of plagioclase (samples 1509GB and 1512MZT6). (**e**) Euhedral corundum porphyroblast with inclusion of relic muscovite, residing in leucosome (sample 1509GB). (**f**) Peritectic euhedral corundum surrounded by a coarse-grained K-feldspar, which encloses remnant grains of biotite (sample 1512MZT6).

The mesosome domains have a weakly foliated fabric mostly defined by subhedral feldspar and interstitial biotite. In most aluminous levels of the gneisses, mesosome domains also contain corundum, occurring as clusters of oriented grains intergrown with alkali feldspar and aligned along the foliation (Figure 4c,d). The preferential orientation of biotite, feldspar and of the small aggregates of corundum + K-feldspar might represent a relic of an earliest foliation. More detailed petrographic observations of the corundum + K-feldspar intergrowths show the occurrence of inclusions of sillimanite and K-feldspar in the small corundum grains, which suggests that the clusters of corundum could be pseudomorphs after former aluminosilicate grains. Sillimanite only occurs as inclusions in corundum (Figure 5a,b).

4.2. Mineral Chemistry

Corundum in sample 1509GB contained more Cr_2O_3 (Cr_2O_3 = 0.04–0.26 wt%) than that in sample 1512MZT6 (Cr_2O_3 = 0.01-0.09 wt%) (Table 2); this resulted in its reddish (1509GB) vs. bluish (1512MZT6) color in the two samples. In the two samples, coarse-grained corundum in the leucosomes and fine-grained corundum in the mesosomes had similar compositions.

Table 2. Electron microprobe analyses of representative minerals from the corundum-bearing rocks in the NDZ.

Wt %	**Sample 1509GB**								**Sample 1512MZT6**								
Mineral	**Bt**		**Crn**		**Kfs**		**Pl**	**Mus**	**Bt**		**Crn**		**Kfs**		**Pl**	**Mus**	**Sill**
Location	**Lc**	**Mo**	**Lc**	**Mo**	**Lc**	**Mo**	**Mo**	**Relic**	**Lc**	**Mo**	**Lc**	**Mo**	**Lc**	**Mo**	**Mo**	**Relic**	**Relic**
SiO_2	36.01	35.52	0.04	0.99	63.72	63.76	60.93	47.45	34.36	35.02	0.00	0.09	65.32	65.28	66.36	47.48	36.12
TiO_2	4.75	3.74	0.01	0.01	0.08	0.05	0.00	0.09	3.87	3.30	0.00	0.04	0.04	0.00	0.00	0.22	0.04
Al_2O_3	19.77	19.81	99.05	98.08	19.58	18.53	23.66	35.86	19.46	19.86	98.74	97.78	18.57	18.57	20.47	37.35	62.67
Cr_2O_3	0.02	0.11	0.12	0.22	0.05	0.00	0.01	0.07	0.06	0.01	0.03	0.00	0.02	0.10	0.00	0.07	0.00
FeO	12.90	12.63	0.39	0.41	0.00	0.00	0.02	0.43	17.31	17.09	0.76	0.73	0.02	0.01	0.06	1.19	0.63
MnO	0.10	0.09	0.02	0.01	0.00	0.00	0.01	0.00	0.15	0.08	0.02	0.00	0.00	0.00	0.06	0.04	0.04
MgO	11.24	12.49	0.00	0.02	0.00	0.02	0.01	0.04	8.79	9.49	0.00	0.00	0.00	0.00	0.02	0.15	0.00
CaO	0.03	0.00	0.02	0.00	0.15	0.08	5.28	0.02	0.00	0.00	0.03	0.06	0.09	0.04	1.14	0.01	0.02
Na_2O	0.34	0.19	0.03	0.04	3.26	1.48	8.18	3.34	0.18	0.14	0.00	0.00	1.64	1.29	10.55	1.72	0.03
K_2O	10.48	10.37	0.04	0.19	12.92	12.76	0.22	7.12	10.36	10.20	0.00	0.02	13.56	13.93	0.36	8.18	0.03
Total	96.08	95.05	99.71	99.95	99.83	96.86	98.32	94.43	94.61	95.39	99.58	98.70	99.47	99.38	99.03	96.41	99.58
								Formulae									
O atoms	11	11	3	3	8	8	8	11	11	11	3	3	8	8	8	11	3
Si	2.405	2.36	0.00	0.03	2.93	3.00	2.75	3.135	2.365	2.37	0.00	0.00	3.00	3.01	2.94	3.065	0.98
Ti	0.24	0.185	0.00	0.00	0.00	0.00	0.00	0.005	0.2	0.17	0.00	0.00	0.00	0.00	0.00	0.01	0.00
Al	1.555	1.55	2.99	2.96	1.06	1.03	1.26	2.79	1.575	1.585	2.98	2.98	1.01	1.01	1.07	2.84	2.00
Fe^{3+}	0	0	0.01	0.01	0.00	0.00	0.00	0	0	0	0.02	0.02	0.00	0.00	0.00	0	0.01
Fe^{2+}	0.72	0.7	0.00	0.00	0.00	0.00	0.00	0.025	0.995	0.965	0.00	0.00	0.00	0.00	0.00	0.065	0.01
Mg	1.12	1.24	0.00	0.00	0.00	0.00	0.00	0.005	0.9	0.955	0.00	0.00	0.00	0.00	0.00	0.015	0.00
Ca	0	0	0.00	0.00	0.01	0.00	0.26	0	0	0	0.00	0.00	0.00	0.00	0.05	0	0.00
Na	0.045	0.025	0.00	0.00	0.29	0.13	0.71	0.43	0.025	0.02	0.00	0.00	0.15	0.12	0.91	0.215	0.00
K	0.895	0.88	0.00	0.00	0.76	0.77	0.01	0.6	0.91	0.88	0.00	0.00	0.80	0.82	0.02	0.675	0.00
Mn	0.005	0.005	0.00	0.00	0.00	0.00	0.00	0	0.01	0.005	0.00	0.00	0.00	0.00	0.00	0	0.00
X_{Mg}	0.305	0.32						0	0.235	0.25							
X_{An}					0.01	0.00	0.26						0.00	0.00	0.06		
X_{Ab}					0.28	0.15	0.73						0.15	0.12	0.92		
X_{Or}					0.72	0.85	0.01						0.84	0.87	0.02		

Lc: in leucosome; Mo: in mesosome.

Muscovite is only found as relic inclusions within corundum porphyroblasts in the leucosome. White mica has Si per 11-oxygen formula unit ranging from 3.0 to 3.14. Biotite commonly occurs in the mesocratic domains or as round inclusions within K-feldspar in the leucosomes. The analyzed biotites displayed high Al (from 1.55 to 1.85 a.p.f.u. on the basis of 11 oxygen) and relatively high Ti contents (Ti = 0.17–0.25 a.p.f.u.); the highest Ti contents were preserved in biotite inclusions in the K-feldspar of leucosome. Fe/(Fe + Mg) in biotite varied from 0.34 to 0.53.

Plagioclase within the matrix is sodium-rich with a compositional range of Ab72-98. Alkali feldspar is generally perthitic and has a X_{Ab} in the range of 0.04–0.34.

5. Discussion

5.1. Anatectic Origin of Corundum

Corundum formation in rocks has been attributed to a wide variety of processes, including primary igneous crystallization, xenocrysts in alkali igneous rocks, metamorphic, metasomatic, and anatectic origins [36,74]. Textural relationships at both the meso- and micro-scale (Figures 4 and 5) and bulk compositions (Table 1) of corundum-bearing rocks in the NDZ clearly exclude the magmatic and metasomatic origin of the corundum. An intimate association between corundum and leucosomes can be observed, with corundum porphyroblasts systematically occurring within the leucosomes (Figure 4a,b). We therefore infer that the corundum formed in situ during anatexis. The anatectic model is in agreement with the large size of corundum in leucosomes, as well as with its euhedral shape.

A number of experimental studies have demonstrated that corundum can be a peritectic phase during partial melting of muscovite in the absence of quartz [75–79]. Experiments in the system K_2O-Al_2O_3-SiO_2-H_2O (KASH), showed that corundum + melt + K-feldspar form through incongruent melting of muscovite under water-absent conditions at pressures of 1.5 GPa at 885 °C [78]. Furthermore, it was demonstrated that, opposite to sub-solidus conditions, under which aluminum is a highly immobile element, Al_2O_3 may rapidly be transported to the surface of growing corundum crystals in the presence of melt [80].

Natural examples of corundum-bearing migmatites have been reported from different localities. Dehydration melting of muscovite with the formation of peritectic corundum, K-feldspar and melt was described by [27] in the Lewisian Complex, North-west Scotland. They reported peritectic melting of aluminous rocks to give corundum-bearing restites and quartz-normative melts at T = 900–925 °C and P > 1.1 GPa. [81] reported the formation of corundum porphyroblasts in anatexites from the Mozambique Belt near Morogoro, in Tanzania. However, they suggested that corundum formed through dehydration of paragonite, according to the reaction: Paragonite = Albite + Corundum + H_2O at T = 695 °C and P = 0.77 GPa. [22] described the corundum-leucosome-bearing aluminous gneiss from Ayyarmalai, Southern Granulite Terrain, India. They thought that corundum is the peritectic product of muscovite dehydration-melting in a silica-undersaturated system within a narrow P-T range of ca. 800 °C and 10–12 kbar. Corundum megacryst-bearing rocks belonging to the Nakkedal Nappe Complex, North Norwegian Caledonides were studied by [44]. They suggested that corundum was formed through the incongruent melting of plagioclase under water-saturated conditions, at temperatures >850 °C and pressure >1.2 GPa. Overall, natural occurrences of corundum-bearing anatectic rocks described so far are the result of high-temperature (amphibolite- to granulite-facies) metamorphism of Al-rich and Si-poor protoliths. These suitable protoliths and P-T conditions occur where passive margins are subducted at continental collision zones. Therefore, corundum-bearing anatectic rocks are considered to be a plate tectonic indicator [74].

5.2. Reaction Microstructures and Petrogenetic Grid

Microstructures and mineral assemblages observed in both the leucosome and mesosome domains point to corundum formation through in situ partial melting involving muscovite breakdown. More specifically:

(i) In the leucosomes, the occurrence of muscovite relics within corundum porphyroblasts suggests that corundum grew at the expense of muscovite. Moreover, textural relationships in the leucosomes (i.e., corundum porphyroblasts systematically occurring in the central part of the leucosomes) are similar to the structures described for granulite-facies migmatites which experienced peritectic melting involving biotite [82–84], where low melt fractions and the absence of differential stresses allowed the anatectic melt to accumulate at the sites of nucleation and growth of peritectic ferromagnesian phases such as garnet, cordierite, and orthopyroxene. By analogy, corundum was interpreted here as the peritectic product of muscovite dehydration melting.

(ii) In the mesosomes, corundum occurs in aggregates of oriented grains intergrown with K-feldspar (Figure 4c,d) and locally includes rounded sillimanite relics rimmed by K-feldspar (Figure 5a,b). [23] described similar microstructures in aluminous gneisses from the central Grenville Province, consisting of resorbed, rounded quartz, rimmed by K-feldspar and included in sillimanite; they suggested that this was evidence for melting involving muscovite breakdown in the presence of quartz, according to the reaction: Muscovite + Quartz ± Plagioclase → Al-silicate + K-feldspar + Liquid, with the Al-silicate formed in the presence of melt. By analogy, we suggest that the clusters of small corundum are the product of the muscovite dehydration melting in the presence of Al-silicate, according to the reaction Muscovite + Al-silicate → Corundum + K-feldspar + Liquid.

Phase relations of metapelite in the NCKFMASH system are largely controlled by the phase relations in the subsystem KFMASH, which in turn is governed by the subsystem KASH. In our samples, aside from the small Mg content of muscovite (see Table 2), biotite is the only ferromagnesian phase which has the passive behavior during melting and the addition of CaO and Na_2O introduces only one phase, plagioclase. Hence, muscovite melting reactions that have occurred in the studied corundum-bearing rocks can be constrained, as a first approximation, using a relatively simple P-T projection in the model system KASH. The petrogenetic grid was calculated with the software PerpleX (version 6.8.6, [85]) using the thermodynamic data set of [86], the equation of state for H_2O of [87,88] and the solution model of [89] for the melt phase.

The calculated P-T projection in the system KASH (Figure 6) shows both quartz-present and quartz-absent equilibria. The main phases considered are muscovite, aluminosilicate, K-feldspar, quartz, corundum, liquid and H_2O. Within the considered P-T range, the topology of equilibria around the invariant points [Crn] and [Qtz] agrees with the chemographies deduced from experimental studies and thermodynamic modeling [78,86]. The calculated P-T projection is also consistent with that published by [22] except for the different location of the [Als, Qtz] absent invariant point, which is likely due to the updated thermodynamic data of [86].

The quartz-absent reaction curves emanating from the invariant point [Qtz] are located at higher temperatures than the quartz-present equilibria and are the key for the interpretation of metamorphic reactions in silica-undersaturated systems. In silica-undersaturated rocks, the sub-solidus dehydration of muscovite occurs through Reaction (1):

$$Ms = Kfs + Crn + H_2O \quad (1)$$

When water is present as a vapour phase, the first melt-producing reaction encountered is the vapour-present muscovite melting with Al-silicate (Reaction (2)),

$$Ms + Als + H_2O = Crn + Melt \quad (2)$$

which occurs at T > 780 °C and produces corundum as a peritectic phase. Under vapour-absent conditions, however, the first voluminous melt-producing reaction is the muscovite dehydration melting with Al-silicate (Reaction (3)),

$$Ms + Als = Kfs + Crn + Melt \quad (3)$$

which occurs at slightly higher temperatures and yields both corundum and K-feldspar as peritectic products. In the absence of Al-silicate, muscovite starts melting at higher temperatures (i.e., T > 840 °C) through Reaction (4), emanating from the [Sil, Qtz] invariant point,

$$Ms = Kfs + Crn + Melt \quad (4)$$

which also produces corundum and K-feldspar as peritectic phases.

The growth of coarse-grained peritectic corundum porphyroblasts hosted in leucosome domains is modeled by the muscovite dehydration melting reaction (Reaction (4): Ms = Kfs + Crn + Melt) at P-T conditions above the [Als, Qtz] invariant point (11 kbar, 840 °C). The clusters of oriented corundum grains intergrown with alkali feldspar occurring in mesocratic domains and the inclusions of sillimanite and K-feldspar in these small corundum grains both suggest that these aggregates of corundum could be pseudomorphs after former aluminosilicate grains. In the KASH system, these microstructures are well explained by the vapour-absent dehydration melting of muscovite with Al-silicate (Reaction (3): Ms + Als = Kfs + Crn + Melt).

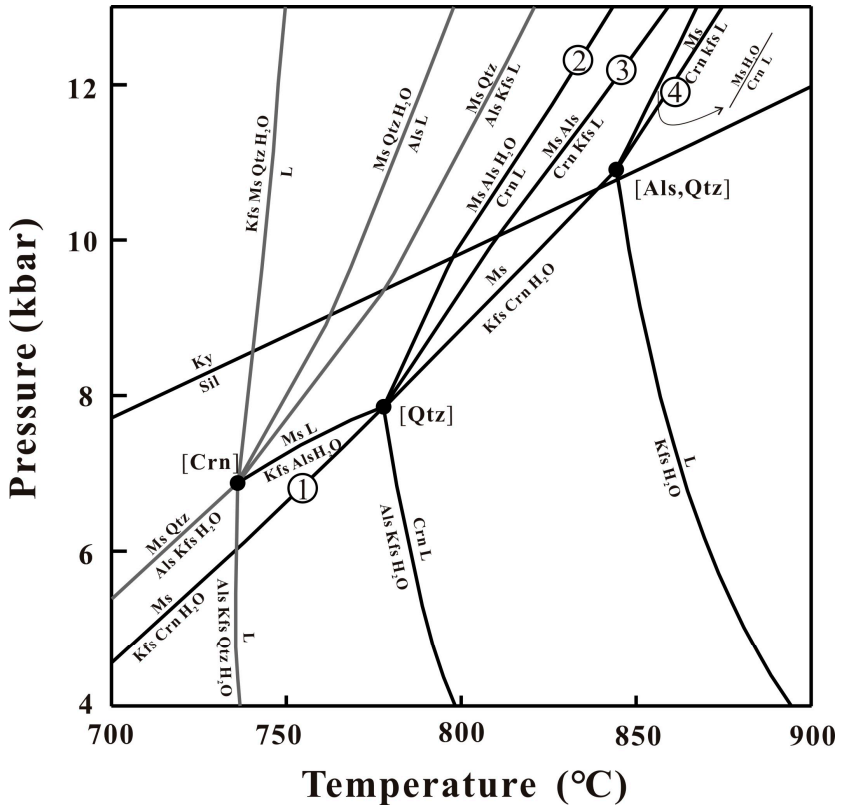

Figure 6. Petrogenetic grid in the system K_2O-Al_2O_3-SiO_2-H_2O showing both quartz-present and quartz-absent equilibria. The anomalous positive slope of reaction Ms + L = Kfs + Als + H_2O that connects the [Qtz] and [Crn] absent invariant points was already documented by [22] and it was explained as the result of uncertainties inherent in the thermodynamic data set; this reaction does not have a significant influence on corundum-bearing rocks. The numbers from 1 to 4 refer to the reactions discussed in the text.

5.3. P-T Pseudosection Modelling and P-T Evolution

Pseudosection modelling provides further insight on the melting reactions and assists in the interpretation of the microstructures. The P-T pseudosection was computed in the system Na_2O-CaO-K_2O-FeO-MgO-Al_2O_3-SiO_2-H_2O-TiO_2 (NCKFMASHT). Fe^{3+} was neglected because Fe^{3+} rich oxides were absent and the amount of Fe^{3+} in the analysed minerals was very low. The phase

diagram was calculated using Perple X (version 6.8.6; [85]), with the updated internally consistent thermodynamic database of [86]. The solid solution models of minerals considered in the calculation were: melt, garnet, biotite and white mica [89], feldspar [90] and spinel [91].

P-T pseudosection was calculated for the sample 1509GB. The effective bulk composition (Table 1) was obtained by combining the mineral proportions obtained from the modal estimate of micro-XRF maps (Figure 3) with mineral chemistry acquired at EPMA (Table 2). The bulk H_2O was calculated based on the proportion of biotite using the H–Ti substitution scheme of [92] (see also [93]). The effective bulk composition was used for the thermodynamic modeling because the determined bulk composition obtained using conventional methods do not provide an accurate estimate of H_2O content. The effective bulk composition based on the mineral proportions obtained from the modal estimate of the XRF map of the whole thin section combined with the mineral chemistry acquired at the EPMA allows a precise estimate of the modal percentage of hydrous minerals (biotite) in the rock.

The P-T pseudosection for sample 1509GB is shown in Figure 7. In this pseudosection, the solidus is predicted at temperature between 740 and 850 °C over the range of modelled pressure (5–15 kbar), although the solidus temperature will vary slightly with any change in H_2O content. The peak phase assemblage in this sample was inferred to have been biotite + K-feldspar + corundum + liquid. Rutile was interpreted as crystallized directly from the melt, because it is idioblastic and exclusively present in the leucosomes. The observed peak phase assemblage was modeled by the broad Crn + L + Bt + Kfs field in Figure 7, at conditions above 870 °C, 6 kbar. The Ti-in biotite isopleths (maximum Ti content of 0.25 a.p.f.u. measured on biotite inclusions in the K-feldspar of leucosome) further constrained peak P-T conditions at ca. 900–950 °C and 9–14 kbar.

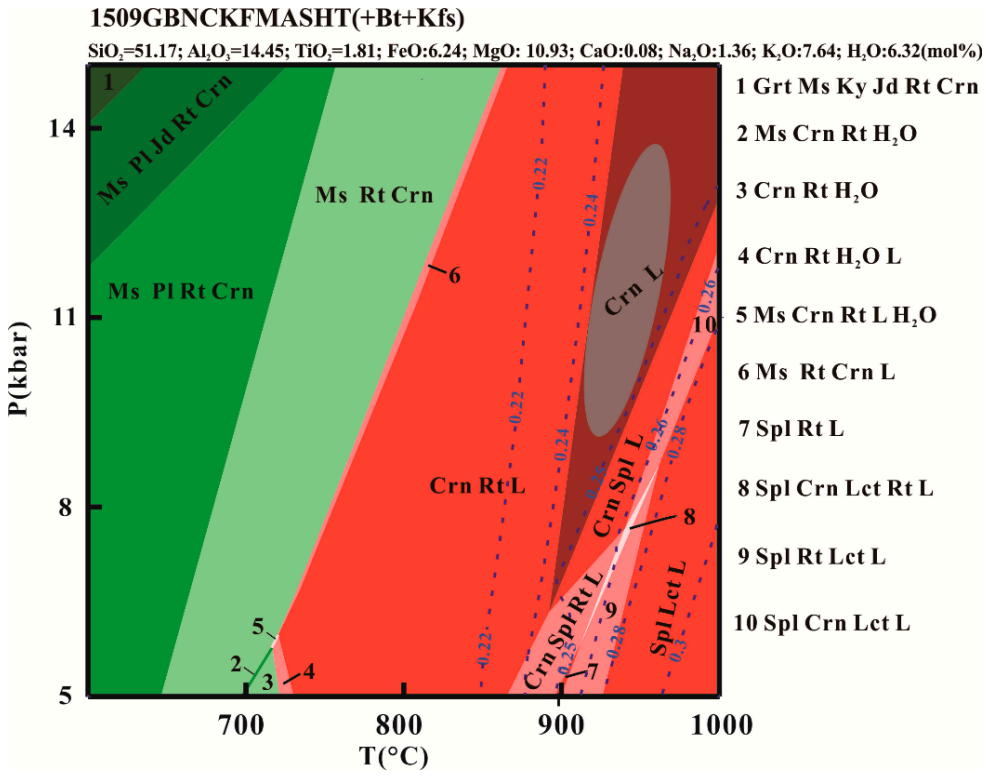

Figure 7. Calculated P-T pseudosections for sample 1509GB. Melt-bearing fields are red, melt absent fields are green. Isopleths of biotite X_{Ti} proportion (in mol%) are reported as blue dotted lines; Gray oval corresponds to the estimated peak condition.

5.4. White Mica Decompression Melting in the NDZ

Dehydration of hydrous minerals is crucial for partial melting of deep continental crust, because in most cases continental crustal rocks, especially in the middle and lower crustal levels, are devoid of free

water. White mica is one of the most common hydrous minerals in continental crustal rocks subducted at depth, being thermodynamically stable in a large pressure range, even at UHP conditions. According to both experimental and thermodynamic studies [7,12], the isothermal decompression of deeply subducted continental crustal slices would cause phengite breakdown, triggering dehydration-driven in situ partial melting of HP/UHP eclogite-facies rocks, now overprinted by granulite-facies assemblages. The positive P-T slopes of the dehydration melting reactions involving phengite and/or muscovite explains why dehydration melting during decompression is a relatively common process during continental collision (i.e., these reactions are systematically crossed during decompression). Based on petrogenetic grids and P-T pseudosections, it has been suggested that up to 40 vol% melt may be produced during isothermal decompression melting assuming a closed system behavior [94]. Even in the case of melt loss episodes, the amount of melt produced during isothermal decompression melting of white mica -bearing rocks should be sufficient to significantly influence the rheological and chemical behavior of continental crust.

The NDZ is an ideal natural laboratory for exploring the importance of white mica decompression melting. In fact, the NDZ underwent a complex metamorphic evolution characterized by repeated episodes of anatexis, resulting in the widespread exposure of migmatites with different generations of granitic leucosomes and dykes [65]. The complex anatectic evolution of the NDZ is mostly related to its retrograde history. The whole retrograde P-T-t evolution of the NDZ was constrained by [63] by applying the Zr-in-rutile and Ti-in-zircon thermometers and zircon U-Pb geochronology on granulitized eclogites. They provided evidence of a multistage high temperature evolution, from UHP eclogite-facies conditions to granulite-facies overprinting. Recently, several studies focusing on the partial melting of NDZ suggest that the NDZ experienced at least two anatectic events [65,70]. The first anatectic event was related to decompression-melting during exhumation in the Triassic, whereas the second anatectic event was related to post-orogenic heating-melting, coeval with the widespread Cretaceous migmatization in the NDZ.

The first, decompression-melting event experienced by the NDZ was constrained based on petrographic observations from the granulitized eclogites, suggesting that, during the initial exhumation in the Triassic, phengite began to melt according to the melting reaction: Phe + Cpx + Qz = melt + San + Grt + Pl [70]. Petrologic modeling constrained this event at pressures of about 20 kbar, for T > 850 °C.

The corundum-bearing gneisses investigated in this study provide additional petrographic and petrologic evidence for white mica decompression melting in the NDZ. We have demonstrated that corundum is a peritectic phase (i.e., it grew in equilibrium with anatectic melt) and is derived from muscovite dehydration melting in a silica-undersaturated system. Petrogenetic grid and P-T pseudosection modeling suggest that the corundum-bearing rocks experienced peak P-T conditions at ca. 900–950 °C and 9–14 kbar, i.e., at lower pressures with respect to those estimated for the granulitized eclogites.

Combining our new data with those obtained for the granulitized eclogites in the area [55,63,70], it is suggested that the white mica decompression melting during exhumation of the NDZ was a long-lasting process occurring on a depth interval of more than 30 km (Figure 8).

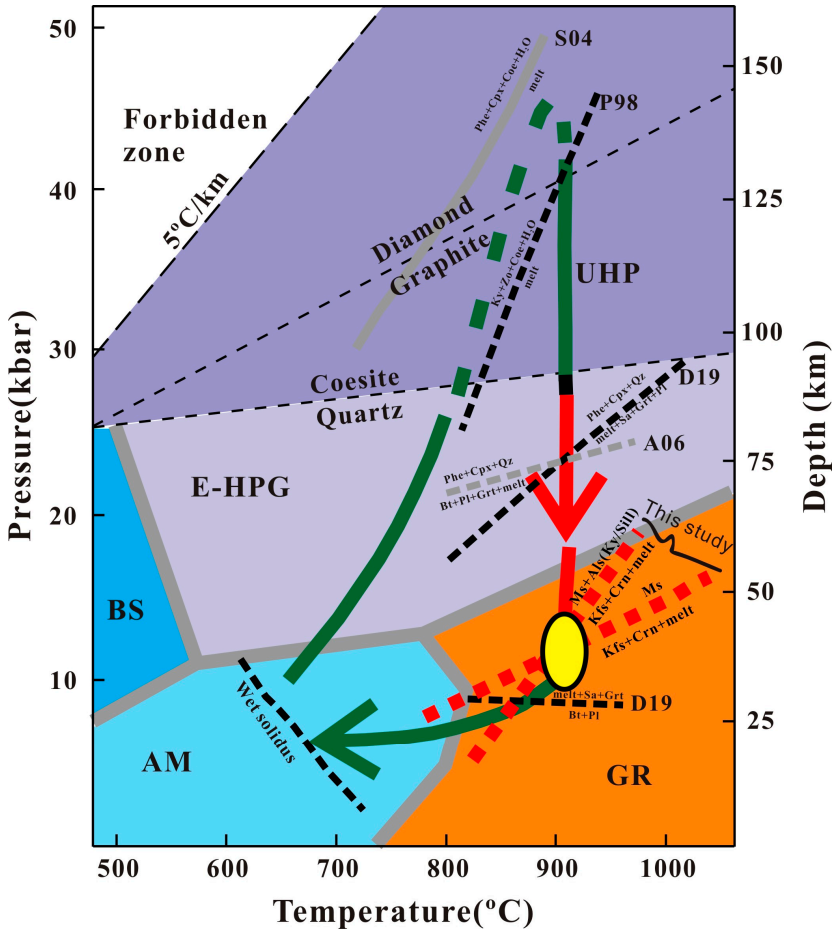

Figure 8. Synthesis of the NDZ P-T path (modified from [70]), with emphasis on the main melt-producing reactions occurred during isothermal decompression, as inferred from previous studies (black and grey dashed curves: S04: [10]; P98, [95]; D19: [70]; A06: [12]) on granulitized eclogites and from this study (red dashed curves) on corundum-bearing anatectic gneisses. The yellow ellipse refers to the peak P-T conditions estimated for the corundum-bearing assemblages.

6. Conclusions

The corundum-bearing rocks in the NDZ provide a classic example of quartz-absent muscovite decompression melting during exhumation of deeply subducted crustal slices. Textural evidence and phase equilibria modeling suggest that corundum was formed by two different muscovite dehydration melting reactions: (1) in the leucosomes, the coarse-grained peritectic corundum grew through the reaction: Ms = Crn + Kfs + Melt; (2) in the mesosomes, the fine-grained corundum + K-feldspar clusters grew through the reaction: Ms + Als = Kfs + Crn + Melt, in the sites of aluminosilicates. P-T pseudosection modeling constrain peak P-T conditions at ca. 900–950 °C, 9–14 kbar, in good agreement with the P-T evolution of the eclogites in the region. These results are robust evidence that the NDZ experienced white mica decompression melting during exhumation, and confirm that partial melting in UHP rocks commonly took place during decompression exhumation.

Author Contributions: Y.L., Y.Y., Y.-C.L., C.G. and F.R. wrote the paper; funding acquisition, Y.-C.L.; field investigation, Y.L., Y.Y. and Y.-C.L.; methodology, Y.L.; project administration, Y.-C.L. All authors have read and agreed to the published version of the manuscript.

Funding: This work was supported by funds from the National Natural Science Foundation of China (41273036 and 41773020).

Acknowledgments: The authors are grateful to Assistant Editor for editor handing and three anonymous reviewers for their many helpful comments and suggestions that greatly helped to improve an earlier version of the manuscript.

Conflicts of Interest: The authors declare no conflicts of interest.

References

1. Korsakov, A.V.; Hermann, J. Silicate and carbonate melt inclusions associated with diamonds in deeply subducted carbonate rocks. *Earth Planet. Sci. Lett.* **2006**, *241*, 104–118. [CrossRef]
2. Labrousse, L.; Duretz, T.; Gerya, T. H_2O-fluid-saturated melting of subducted continental crust facilitates exhumation of ultrahigh-pressure rocks in continental subduction zones. *Earth Planet Sci. Lett.* **2015**, *428*, 151–161. [CrossRef]
3. Stepanov, A.S.; Hermann, J.; Korsakov, A.V.; Rubatto, D. Geochemistry of ultrahigh-pressure anatexis: Fractionation of elements in the Kokchetav gneisses during melting at diamond-facies conditions. *Contrib. Mineral. Petrol.* **2014**, *167*, 1002–1263. [CrossRef]
4. Liu, Y.C.; Deng, L.P.; Gu, X.F. Multistage exhumation and partial melting of high-Tultrahigh-pressure metamorphic rocks in continental subduction-collision zones. *Sci. China Earth Sci.* **2015**, *58*, 1084–1099. [CrossRef]
5. Deng, L.P.; Liu, Y.C.; Gu, X.F.; Groppo, C.; Rolfo, F. Partial melting of ultrahigh-pressure metamorphic rocks at convergent continental margins: Evidences, melt compositions and physical effects. *Geosci. Front.* **2018**, *9*, 1229–1242. [CrossRef]
6. Ferrero, S.; Wunder, B.; Walczak, K.; O'Brien, P.J.; Ziemann, M.A. Preserved near ultrahigh-pressure melt from continental crust subducted to mantle depths. *Geology* **2015**, *43*, 447–450. [CrossRef]
7. Hermann, J.; Green, D.H. Experimental constraints on high pressure melting in subducted crust. *Earth Planet Sci. Lett.* **2001**, *188*, 149–168. [CrossRef]
8. Vanderhaeghe, O.; Teyssier, C. Partial melting and flow of orogens. *Tectonophysics* **2001**, *342*, 451–472. [CrossRef]
9. Visonà, D.; Lombardo, B. Two-mica and tourmaline leucogranites from the Everest-Makalu region (Nepal-Tibet). Himalayan leucogranite genesis by isobaric heating? *Lithos* **2002**, *62*, 125–150. [CrossRef]
10. Schmidt, M.W.; Vielzeuf, D.; Auzanneau, E. Melting and dissolution of subducting crust at high pressures: The key role of white mica. *Earth Planet Sci. Lett.* **2004**, *228*, 65–84. [CrossRef]
11. Whitney, D.L.; Teyssier, C.; Fayon, A.K. Isothermal decompression, partial melting and exhumation of deep continental crust. In *Vertical Coupling and Decoupling in the Lithosphere*; Grocott, J., McCaffrey, K.J.W., Taylor, G., Tikoff, B., Eds.; The Geological Society: London, UK, 2004; Volume 227, pp. 313–326. [CrossRef]
12. Auzanneau, E.; Vielzeuf, D.; Schmidt, M.W. Experimental evidence of decompression melting during exhumation of subducted continental crust. *Contrib. Mineral. Petrol.* **2006**, *152*, 125–148. [CrossRef]
13. Brown, M. Melting of the continental crust during orogenesis: The thermal, rheological, and compositional consequences of melt transport from lower to upper continental crust. *Can. J. Earth Sci.* **2010**, *47*, 655–694. [CrossRef]
14. Groppo, C.; Rolfo, F.; Indares, A. Partial Melting in the Higher Himalayan crystallines of Eastern Nepal: The effect of decompression and implications for the 'channel flow' model. *J. Petrol.* **2012**, *53*, 1057–1088. [CrossRef]
15. Vielzeuf, D.; Holloway, J.R. Experimental-determination of the fluid-absent melting relations in the pelitic system—Consequences for crustal differentiation. *Contrib. Mineral. Petrol.* **1988**, *98*, 257–276. [CrossRef]
16. Mogk, D.W. Ductile shearing and migmatization at mid-crustal levels in an Archaean high-grade gneiss belt, northern Gallatin Range, Montana, USA. *J. Metamorph. Geol.* **1992**, *10*, 427–438. [CrossRef]
17. Stevens, G.; Clemens, J. Fluid-absent melting and the roles of fluids in the lithosphere: A slanted summary? *Chem. Geol.* **1993**, *108*, 1–17. [CrossRef]
18. Sawyer, E.W. Migmatites formed by water-fluxed partial melting of a leucogranodiorite protolith: Microstructures in the residual rocks and source of the fluid. *Lithos* **2010**, *116*, 273–286. [CrossRef]
19. Weinberg, R.F.; Hasalová, P. Water-fluxed melting of the continental crust: A review. *Lithos* **2015**, *212*, 158–188. [CrossRef]

20. Brown, M. Crustal melting and melt extraction, ascent and emplacement in orogens: Mechanisms and consequences. *J. Geol. Soc.* **2007**, *164*, 709–730. [CrossRef]
21. Dyck, B.; Waters, D.J.; St-Onge, M.R.; Searle, M.P. Muscovite dehydration melting: Reaction mechanisms, microstructures, and implications for anatexis. *J. Metamorph. Geol.* **2019**. [CrossRef]
22. Raith, M.M.; Sengupta, P.; Kooijman, E.; Upadhyay, D.; Srikantappa, C. Corundum-leucosome-bearing aluminous gneiss from Ayyarmalai, Southern Granulite Terrain, India: A textbook example of vapor phase-absent muscovite-melting in silica-undersaturated aluminous rocks. *Am. Mineral.* **2010**, *95*, 897–907. [CrossRef]
23. Lasalle, S.; Indares, A. Anatectic record and contrasting P–T paths of aluminous gneisses from the central Grenville Province. *J. Metamorph. Geol.* **2014**, *32*, 627–646. [CrossRef]
24. Breton, N.L.; Thompson, A.B. Fluid-absent (dehydration) melting of biotite in metapelites in the early stages of crustal anatexis. *Contrib. Mineral. Petrol.* **1988**, *99*, 226–237. [CrossRef]
25. Brown, M.; Sawyer, E. Granites, migmatites and residual granulites: Relationships and processes. In *Working with Migmatites*; Sawyer, E.W., Brown, M., Eds.; Short Course Series; Mineralogical Association of Canada: Québec, QC, Canada, 2008; Volume 38, pp. 97–144.
26. Grant, J.A. Phase-equilibria in low-pressure partial melting of pelitic rocks. *Am. J. Sci.* **1985**, *285*, 409–435. [CrossRef]
27. Cartwright, I.; Barnicoat, A. The generation of quartz-normative melts and corundum-bearing restites by crustal anatexis: Petrogenetic modelling based on an example from the Lewisian of North-West Scotland. *J. Metamorph. Geol.* **1986**, *4*, 79–99. [CrossRef]
28. Pattison, D.; Harte, B. Petrography and mineral chemistry of pelites. In *Equilibrium and Kinetics in Contact Metamorphism*; Springer: Berlin/Heidelberg, Germany, 1991; pp. 135–179.
29. Riesco, M.; Stuwe, K.; Reche, J.; Martinez, F.J. Silica depleted melting of pelites. petrogenetic grid and application to the Susqueda Aureole, Spain. *J. Metamorph. Geol.* **2004**, *22*, 475–494. [CrossRef]
30. Kelsey, D.E.; White, R.W.; Powell, R. Calculated phase equilibria in K_2O-FeO-MgO-Al_2O_3-SiO_2-H_2O for silica-undersaturated sapphire-bearing mineral assemblages. *J. Metamorph. Geol.* **2005**, *23*, 217–239. [CrossRef]
31. Kelsey, D.E. On ultrahigh-temperature crustal metamorphism. *Gondwana Res.* **2008**, *13*, 1–29. [CrossRef]
32. Dorfler, K.M.; Caddick, M.J.; Tracy, R.J. Thermodynamic modeling of crustal melting using xenolith analogs from the cortlandt complex, New York, USA. *J. Petrol.* **2015**, *56*, 389–408. [CrossRef]
33. Guevara, V.; Caddick, M. Shooting at a moving target: Phase equilibria modelling of high-temperature metamorphism. *J. Metamorph. Geol.* **2016**, *34*, 209–235. [CrossRef]
34. Keller, D.S.; Ague, J.J. High-pressure granulite facies metamorphism (similar to 1.8 GPa) revealed in silica-undersaturated garnet-spinel-corundum gneiss, Central Maine Terrane, Connecticut, USA. *Am. Mineral.* **2018**, *103*, 1851–1868. [CrossRef]
35. Giuliani, G.; Ohnenstetter, D.; Fallick, A.; Groat, L.; Fagan, A.J. The geology and genesis of gem corundum deposits. In *Geology of Gem Deposits*; Groat, L.A., Ed.; Mineralogical Association of Canada: Tucson, AZ, USA, 2014; pp. 29–112.
36. Simonet, C.; Fritsch, E.; Lasnier, B. A classification of gem corundum deposits aimed towards gem exploration. *Ore. Geol. Rev.* **2008**, *34*, 127–133. [CrossRef]
37. Bottrill, R.S. A corundum-quartz assemblage in altered volcanic rocks, Bond Range, Tasmania. *Mineral. Mag.* **1998**, *62*, 325–332. [CrossRef]
38. Zhang, Z.M.; Ding, H.X.; Dong, X.; Tian, Z.L.; Mu, H.C.; Li, M.M.; Qin, S.K.; Niu, Z.X.; Zhang, N. The eocene corundum-bearing rocks in the gangdese arc, South Tibet: Implications for tectonic evolution of the Himalayan orogen. *Geosci. Front.* **2018**, *9*, 1337–1354. [CrossRef]
39. Sorokina, E.S.; Rassomakhin, M.A.; Nikandrov, S.N.; Karampelas, S.; Kononkova, N.N.; Nikolaev, A.G.; Anosova, M.O.; Somsikova, A.V.; Kostitsyn, Y.A.; Kotlyarov, V.A. Origin of blue sapphire in newly discovered spinel–chlorite–muscovite rocks within meta-ultramafites of Ilmen Mountains, South Urals of Russia: Evidence from mineralogy, geochemistry, Rb-Sr and Sm-Nd isotopic data. *Minerals* **2019**, *9*, 36. [CrossRef]
40. Riesco, M.; Stuwe, K.; Reche, J. Formation of corundum in metapelites around ultramafic bodies. An example from the Saualpe region, Eastern Alps. *Mineral. Petrol.* **2005**, *83*, 1–25. [CrossRef]

41. Yakymchuk, C.; Szilas, K. Corundum formation by metasomatic reactions in Archean metapelite, SW Greenland: Exploration vectors for ruby deposits within high-grade greenstone belts. *Geosci. Front.* **2018**, *9*, 727–749. [CrossRef]
42. Voudouris, P.; Mavrogonatos, C.; Graham, I.; Giuliani, G.; Melfos, V.; Karampelas, S.; Karantoni, V.; Wang, K.; Tarantola, A.; Zaw, K.; et al. Gem corundum deposits of Greece: Geology, mineralogy and genesis. *Minerals* **2019**, *9*, 49. [CrossRef]
43. Palke, A.C.; Renfro, N.D.; Berg, R.B. Melt inclusions in alluvial sapphires from Montana, USA: Formation of sapphires as a restitic component of lower crustal melting? *Lithos* **2017**, *278–281*, 43–53. [CrossRef]
44. Kullerud, K.R.; Nasipuri, P.; Ravna, E.J.K.; Selbekk, R.S. Formation of corundum megacrysts during H_2O-saturated incongruent melting of feldspar: P–T pseudosection-based modelling from the Skattøra migmatite complex, North Norwegian Caledonides. *Contrib. Mineral. Petrol.* **2012**, *164*, 627–641. [CrossRef]
45. Li, S.G.; Xiao, Y.L.; Liou, D.L.; Chen, Y.Z.; Ge, N.J.; Zhang, Z.Q.; Sun, S.S.; Cong, B.L.; Zhang, R.Y.; Hart, S.R. Collision of the North China and yangtse blocks and formation of coesite-bearing eclogites: Timing and processes. *Chem. Geol.* **1993**, *109*, 89–111. [CrossRef]
46. Xu, S.T.; Wen, S.; Yican, L.; Laili, J.; Shouyuan, J.; Okay, A.I.; Sengor, A.M. Diamond from the dabie shan metamorphic rocks and its implication for tectonic setting. *Science* **1992**, *256*, 80–82. [CrossRef]
47. Okay, A.I.; Xu, S.T.; Sengor, A.M.C. Coesite from the Dabie Shan eclogites, Central China. *Eur. J. Mineral.* **1989**, *1*, 595–598. [CrossRef]
48. Wang, X.M.; Liou, J.G.; Mao, H.K. Coesite-bearing eclogite from the Dabie mountains in central China. *Geology* **1989**, *17*, 1085–1088. [CrossRef]
49. Xu, S.T.; Liu, Y.C.; Chen, G.; Compagnoni, R.; Rolfo, F.; He, M.; Liu, H. New finding of micro-diamonds in eclogites from Dabie-Sulu region in central-eastern China. *Sci. Bull.* **2003**, *48*, 988–994. [CrossRef]
50. Xu, S.T.; Liu, Y.C.; Chen, G.B.; Ji, S.Y.; Ni, P.; Xiao, W.S. Microdiamonds, their classification and tectonic implications for the host eclogites from the Dabie and Su-Lu regions in central eastern China. *Mineral. Mag.* **2005**, *69*, 509–520. [CrossRef]
51. Liu, Y.C.; LI, S.G.; Gu, X.F.; Xu, S.T.; Chen, G.B. Ultrahigh-pressure eclogite transformed from mafic granulite in the Dabie orogen, east-central China. *J. Metamorph. Geol.* **2007**, *25*, 975–989. [CrossRef]
52. Li, Y.; Liu, Y.C.; Yang, Y.; Deng, L.P. New U-Pb Geochronological Constraints on Formation and Evolution of the Susong Complex Zone in the Dabie Orogen. *Acta Geol. Sin. Engl.* **2017**, *91*, 1915–1918. [CrossRef]
53. Liu, Y.C.; Liu, L.-X.; Li, Y.; Gu, X.-F.; Song, B. Zircon U-Pb geochronology and petrogenesis of metabasites from the western Beihuaiyang zone in the Hong'an orogen, central China: Implications for detachment within subducting continental crust at shallow depths. *J. Asian Earth Sci.* **2017**, *145*, 74–90. [CrossRef]
54. Xu, S.T.; Wu, W.P.; Lu, Y.Q.; Wang, D.H. Tectonic setting of the low-grade metamorphic rocks of the Dabie Orogen, central eastern China. *J. Struct. Geol.* **2012**, *37*, 134–149. [CrossRef]
55. Groppo, C.; Rolfo, F.; Liu, Y.C.; Deng, L.P.; Wang, A.D. PT evolution of elusive UHP eclogites from the luotian dome (North Dabie zone, China): How far can the thermodynamic modeling lead us? *Lithos* **2015**, *226*, 183–200. [CrossRef]
56. Li, S.G.; Jagoutz, E.; Chen, Y.Z.; Li, Q.L. Sm-Nd and Rb-Sr isotopic chronology and cooling history of ultrahigh pressure metamorphic rocks and their country rocks at Shuanghe in the Dabie mountains, central China. *Geochim. Cosmochim. Acta* **2000**, *64*, 1077–1093. [CrossRef]
57. Liu, Y.C.; Li, S.G.; Xu, S.T.; Jahn, B.M.; Zheng, Y.F.; Zhang, Z.Q.; Jiang, L.L.; Chen, G.B.; Wu, W.P. Geochemistry and geochronology of eclogites from the northern Dabie Mountains, central China. *J. Asian Earth Sci.* **2005**, *25*, 431–443. [CrossRef]
58. Liu, Y.C.; Gu, X.F.; Rolfo, F.; Chen, Z.Y. Ultrahigh-pressure metamorphism and multistage exhumation of eclogite of the Luotian dome, North Dabie Complex Zone (central China): Evidence from mineral inclusions and decompression textures. *J. Asian Earth Sci.* **2011**, *42*, 607–617. [CrossRef]
59. Okay, A.I. Petrology of a diamond and coesite-bearing metamorphic terrain—Dabie Shan, China. *Eur. J. Mineral.* **1993**, *5*, 659–675. [CrossRef]
60. Rolfo, F.; Compagnoni, R.; Wu, W.; Xu, S. A coherent lithostratigraphic unit in the coesite–eclogite complex of Dabie Shan, China: Geologic and petrologic evidence. *Lithos* **2004**, *73*, 71–94. [CrossRef]
61. Liu, Y.C.; Deng, L.P.; Gu, X.F.; Chiara, G.; Franco, R. Multistage metamorphic evolution and P-T-t Path of high-T eclogite from the North Dabie Complex Zone during continental subduction and exhumation. *Acta Geol. Sin. Engl.* **2016**, *90*, 759–760. [CrossRef]

62. Liu, Y.C.; Li, S. Detachment within subducted continental crust and multi-slice successive exhumation of ultrahigh-pressure metamorphic rocks: Evidence from the Dabie-Sulu orogenic belt. *Chin. Sci. Bull.* **2008**, *53*, 3105–3119. [CrossRef]
63. Liu, Y.C.; Deng, L.P.; Gu, X.F.; Groppo, C.; Rolfo, F. Application of Ti-in-zircon and Zr-in-rutile thermometers to constrain high-temperature metamorphism in eclogites from the Dabie orogen, central China. *Gondwana Res.* **2015**, *27*, 410–423. [CrossRef]
64. Liu, Y.C.; Li, S.G.; Xu, S.T. Zircon Shrimp U–Pb dating for gneisses in northern Dabie high T/P metamorphic zone, central China: Implications for decoupling within subducted continental crust. *Lithos* **2007**, *96*, 170–185. [CrossRef]
65. Liu, Y.C.; Yang, Y.; Li, Y. New constraints on multiple anatexis in the North Dabie complex zone and mountain-root collapse in the Dabie Orogen, central China. *Chin. J. Geol.* **2019**, *54*, 664–677.
66. Wang, J.H.; Sun, M.; Deng, S.X. Geochronological constraints on the timing of migmatization in the Dabie Shan, East-central China. *Eur. J. Mineral.* **2002**, *14*, 513–524. [CrossRef]
67. Wang, S.J.; Li, S.G.; Chen, L.J.; He, Y.S.; An, S.C.; Shen, J. Geochronology and geochemistry of leucosomes in the North Dabie Terrane, East China: Implication for post-UHPM crustal melting during exhumation. *Contrib. Mineral. Petrol.* **2013**, *165*, 1009–1029. [CrossRef]
68. Malaspina, N.; Hermann, J.; Scambelluri, M.; Compagnoni, R. Multistage metasomatism in ultrahigh-pressure mafic rocks from the North Dabie Complex (China). *Lithos* **2006**, *90*, 19–42. [CrossRef]
69. Liu, Y.C.; Gu, X.F.; Li, S.G.; Hou, Z.H.; Song, B. Multistage metamorphic events in granulitized eclogites from the North Dabie complex zone, central China: Evidence from zircon U–Pb age, trace element and mineral inclusion. *Lithos* **2011**, *122*, 107–121. [CrossRef]
70. Deng, L.P.; Liu, Y.C.; Yang, Y.; Groppo, C.; Rolfo, F.; Gu, X.F. Anatexis of high-T eclogites in the Dabie orogen triggered by exhumation and post-orogenic collapse. *Eur. J. Mineral.* **2019**, *31*, 889–903. [CrossRef]
71. Tsai, C.-H.; Liou, J.G. Eclogite-facies relics and inferred ultrahigh-pressure metamorphism in the North Dabie Complex, central-eastern China. *Am. Mineral.* **2000**, *85*, 1–8. [CrossRef]
72. Yang, Y.; Liu, Y.C.; Li, Y.; Groppo, C.; Rolfo, F.; Deng, L.P.; Song, B. Time and petrogenesis of different generations of leucosomes in the North Dabie complex zone, central China: New constraints on multiple episodes of anatexis. unpulished.
73. Whitney, D.L.; Evans, B.W. Abbreviations for names of rock-forming minerals. *Am. Mineral.* **2010**, *95*, 185–187. [CrossRef]
74. Stern, R.J.; Tsujimori, T.; Harlow, G.; Groat, L.A. Plate tectonic gemstones. *Geology* **2013**, *41*, 723–726. [CrossRef]
75. Evans, B. Application of a reaction-rate method to the breakdown equilibria of muscovite and muscovite plus quartz. *Am. J. Sci.* **1965**, *263*, 647–667. [CrossRef]
76. Huang, W.L.; Robertson, J.K.; Wyllie, P.J. Melting relations of muscovite to 30 kilobars in the system $KAlSi_3O_8$-Al_2O_3 -H_2O. *Am. J. Sci.* **1973**, *273*, 415–427. [CrossRef]
77. Huang, W.L.; Wyllie, P.J. Muscovite dehydration and melting in deep crust and subducted oceanic sediments. *Earth Planet Sci. Lett.* **1973**, *18*, 133–136. [CrossRef]
78. Huang, W.L.; Wyllie, P.J. Melting relations of muscovite with quartz and sanidine in the K_2O-Al_2O_3-SiO_2-H_2O system to 30 kilobars and an outline of paragonite melting relations. *Am. J. Sci.* **1974**, *274*, 378–395. [CrossRef]
79. Velde, B. Upper stability of muscovite. *Am. Mineral.* **1966**, *51*, 924–929.
80. Newton, R.C.; Manning, C.E. Solubility of corundum in the system Al_2O_3–SiO_2–H_2O–NaCl at 800 °C and 10 kbar. *Chem. Geol.* **2008**, *249*, 250–261. [CrossRef]
81. Altherr, R.; Okrusch, M.; Bank, H. Corundum-and kyanite-bearing anatexites from the Precambrian of Tanzania. *Lithos* **1982**, *15*, 191–197. [CrossRef]
82. Powell, R.; Downes, J. Garnet porphyroblast-bearing leucosomes in metapelites: Mechanisms, phase diagrams, and an example from Broken Hill, Australia. In *High-Temperature Metamorphism and Crustal Anatexis*; Springer: Berlin/Heidelberg, Germany, 1990; pp. 105–123.
83. Braun, I.; Raith, M.; Kumar, G.R.R. Dehydration—melting phenomena in leptynitic gneisses and the generation of leucogranites: A case study from the kerala khondalite belt, Southern India. *J. Petrol.* **1996**, *37*, 1285–1305. [CrossRef]
84. White, R.W.; Powell, R.; Halpin, J. Spatially-focussed melt formation in aluminous metapelites from Broken Hill, Australia. *J. Metamorph. Geol.* **2005**, *22*, 825–845. [CrossRef]

85. Connolly, J.A.D. Computation of phase equilibria by linear programming: A tool for geodynamic modeling and its application to subduction zone decarbonation. *Earth Planet. Sci. Lett.* **2005**, *236*, 524–541. [CrossRef]
86. Holland, T.J.B.; Powell, R. An improved and extended internally consistent thermodynamic dataset for phases of petrological interest, involving a new equation of state for solids. *J. Metamorph. Geol.* **2011**, *29*, 333–383. [CrossRef]
87. Holland, T.J.B.; Powell, R. An internally consistent thermodynamic data set for phases of petrological interest. *J. Metamorph. Geol.* **1998**, *16*, 309–343. [CrossRef]
88. Kelsey, D.; White, R.; Holland, T.; Powell, R. Calculated phase equilibria in K_2O-FeO-MgO-Al_2O_3-SiO_2-H_2O for sapphirine-quartz-bearing mineral assemblages. *J. Metamorph. Geol.* **2004**, *22*, 559–578. [CrossRef]
89. White, R.W.; Powell, R.; Holland, T.J.B.; Johnson, T.E.; Green, E.C.R. New mineral activity–composition relations for thermodynamic calculations in metapelitic systems. *J. Metamorph. Geol.* **2014**, *32*, 261–286. [CrossRef]
90. Fuhrman, M.L.; Lindsley, D.H. Ternary-Feldspar modeling and thermometry. *Am. Mineral.* **1988**, *73*, 201–215.
91. White, R.W.; Powell, R.; Clarke, G.L. The interpretation of reaction textures in Fe-rich metapelitic granulites of the Musgrave Block, central Australia: Constraints from mineral equilibria calculations in the system K_2O-FeO-MgO-Al_2O_3-SiO_2-H_2O-TiO_2-Fe_2O_3. *J. Metamorph. Geol.* **2002**, *20*, 41–55. [CrossRef]
92. White, R.W.; Powell, R.; Holland, T.J.B. Progress relating to calculation of partial melting equilibria for metapelites. *J. Metamorph. Geol.* **2007**, *25*, 511–527. [CrossRef]
93. Groppo, C.; Rolfo, F.; Mosca, P. The cordierite-bearing anatectic rocks of the higher Himalayan crystallines (eastern Nepal): Low-pressure anatexis, melt productivity, melt loss and the preservation of cordierite. *J. Metamorph. Geol.* **2013**, *31*, 187–204. [CrossRef]
94. Spear, F.S.; Kohn, M.J.; Cheney, J.T. P-T paths from anatectic pelites. *Contrib. Mineral. Petrol.* **1999**, *134*, 17–32. [CrossRef]
95. Poli, S.; Schmidt, M.W. The high-pressure stability of zoisite and phase relationships of zoisite-bearing assemblages. *Contrib. Mineral. Petrol.* **1998**, *130*, 162–175. [CrossRef]